



Dynamic microscale flow patterning using electrical modulation of zeta potential

Federico Paratore^{a,b,c}, Vesna Bacheva^a, Govind V. Kaigala^{a,1}, and Moran Bercovic^{b,c,1}

^aIBM Research–Zurich, 8803 Rüschlikon, Switzerland; ^bFaculty of Mechanical Engineering, Technion–Israel Institute of Technology, 3200003 Haifa, Israel; and ^cDepartment of Mechanical Engineering, The University of Texas at Austin, Austin, TX 78712

Edited by David A. Weitz, Harvard University, Cambridge, MA, and approved March 7, 2019 (received for review January 2, 2019)

The ability to move fluids at the microscale is at the core of many scientific and technological advancements. Despite its importance, microscale flow control remains highly limited by the use of discrete channels and mechanical valves, and relies on fixed geometries. Here we present an alternative mechanism that leverages localized field-effect electroosmosis to create dynamic flow patterns, allowing fluid manipulation without the use of physical walls. We control a set of gate electrodes embedded in the floor of a fluidic chamber using an ac voltage in sync with an external electric field, creating nonuniform electroosmotic flow distributions. These give rise to a pressure field that drives the flow throughout the chamber. We demonstrate a range of unique flow patterns that can be achieved, including regions of recirculating flow surrounded by quiescent fluid and volumes of complete stagnation within a moving fluid. We also demonstrate the interaction of multiple gate electrodes with an externally generated flow field, allowing spatial modulation of streamlines in real time. Furthermore, we provide a characterization of the system in terms of time response and dielectric breakdown, as well as engineering guidelines for its robust design and operation. We believe that the ability to create tailored microscale flow using solid-state actuation will open the door to entirely new on-chip functionalities.

electrokinetics | microfluidics | electroosmotic flow | viscous flow | Hele–Shaw cell

Manipulation of fluids at the microscale is important for a wide range of applications, from laboratory-on-a-chip devices (1), through adaptive optics (2, 3), to energy harvesting (4, 5). Whereas two-phase flows can be controlled by acting on a fluid–fluid interface through a variety of physical mechanisms [e.g., electrowetting on dielectric (6), dielectrophoresis (7), and thermocapillary (8)], control of continuous-phase flows at the microscale, lacking such an interface, remains a significant challenge.

At present, routing single-phase flows through desired flow paths is obtained primarily by the use of solid channels, constraining the types of flows that can be achieved. The development of on-chip valves (9) increased the flexibility of routing fluids on a large scale, allowing complex and dynamic fluid manipulation through microfluidic networks. However, valve-based platforms still rely on fixed-channel geometries, are limited to discrete actuation, and are not easily scalable.

Electroosmotic flow (EOF) is the motion of an electrolyte resulting from the interaction of an external electric field with the net charge of an electric double layer (EDL). Recently, Boyko et al. (10) suggested theoretically that nonuniform EOF can be used to achieve desired flow patterns in planar configurations. Paratore et al. (11) experimentally demonstrated this concept using chemical patterning of the surface by deposition of polyelectrolytes. Because the zeta-potential pattern is obtained by chemical modification, this approach can only generate static flow fields. Moreover, the number of flow patterns that can be created is severely limited by the discrete number of zeta potential that can be prescribed (i.e., number of available polyelectrolytes).

An alternative approach to control the EOF relies on the application of a perpendicular electric field to the surface, thus enabling modification of the zeta potential in a dynamic fashion. The use of an external dc field for modifying zeta potential was

first proposed by Ghowsi and Gale (12) and demonstrated experimentally by Lee et al. (13) in the context of capillary electrophoresis to reduce band broadening and adsorption of analytes on capillary walls (14–16). Schasfoort et al. (17) were the first to implement this approach on-chip and propose it as a controlling and switching element in microfluidic networks, followed by several works exploring the effect of different dielectric layers (17–21). Several names were proposed for this phenomenon including “flow field-effect transistor (flowFET)” (17) and “field-effect flow control” (18); herein we will refer to it as “field-effect electroosmosis” or FEEO as it best captures the physical phenomenon, as was originally proposed in 1989 by Ghowsi and Gale (12).

FEEO is most effective when working at pH values close to the point of zero charge of the substrate, at which the native zeta potential of the surface is approximately zero, and the field effect becomes predominant. At higher or lower pHs, FEEO has a smaller contribution relative to the native surface potential (22). Moreover, because the process is driven by a dc electric field, gas bubble due to electrolysis can limit its use, and the fluid flow cannot be used to directly dictate the motion of molecules and particles in the liquid as those also experience electrophoretic migration. While for native surfaces an ac driving field would lead to a zero time-averaged EOF, Muthu et al. (23) showed that by synchronizing the phase of a gate electrode with that of the driving field, a net flow in a desired direction can be obtained. More recently, van der Wouden et al. (24, 25) investigated the time response of such systems and demonstrated its application to microfluidic pumping.

Here we report the use of ac-FEEO as a mechanism for dynamic control of spatial flow patterns in microfluidic chambers. Using a discrete disk-shaped gate electrode, we first reproduce the EOF dipole predicted by Boyko et al. (10). In contrast to chemical patterning (11), which has a fixed zeta-potential distribution, we show that the use of ac-FEEO allows a continuous

Significance

Traditional microfluidic devices make use of physical channels and mechanical actuators, in which geometries and functionalities are intimately related to one another, i.e., changing the flow field requires change at the mechanical level. In this work, we introduce a concept in which a microfluidic chamber with no preset structures or active mechanical components can be dynamically configured to produce desired flow fields.

Author contributions: F.P., V.B., G.V.K., and M.B. conceived the research; F.P. and V.B. performed the experiments; F.P. and V.B. analyzed data; F.P. and V.B. compared experimental data to the analytical model; F.P. fabricated the devices; F.P., V.B., G.V.K., and M.B. discussed the data; and F.P. and M.B. wrote the paper with input from all authors.

The authors declare no conflict of interest.

This article is a PNAS Direct Submission.

This open access article is distributed under [Creative Commons Attribution License 4.0 \(CC BY\)](https://creativecommons.org/licenses/by/4.0/).

¹To whom correspondence may be addressed. Email: gov@zurich.ibm.com or mberco@technion.ac.il.

This article contains supporting information online at www.pnas.org/lookup/suppl/doi/10.1073/pnas.1821269116/-DCSupplemental.

Published online May 6, 2019.

range of zeta-potential values to be prescribed, thus enabling the flow field to be tuned in real time. We characterize the dielectric breakdown threshold for a range of dielectric materials and investigate the time response of our devices, providing engineering guidelines for the design of such systems. We then demonstrate the use of various electrode configurations for dynamically shaping microscale flows, creating dipoles, quadrupoles, and isolated flow regions, as well as the deformation of pressure-generated streamlines.

Concept of Flow Patterning Using ac-FEEO

As illustrated in Fig. 1, we use a Hele–Shaw chamber of thickness h and length L filled with an electrolyte in direct contact with a ground electrode and a driving electrode (Fig. 1A). The floor of the chamber contains an embedded electrode (gate electrode) with a characteristic dimension r_0 , located at a distance x_{el} from the ground electrode. The gate electrode is electrically insulated from the electrolyte by a dielectric layer of thickness d and dielectric constant ϵ_d (Fig. 1B). We actuate both the driving and the gate electrode with an ac potential at a frequency ω and amplitudes ϕ_i , $V_i(t) = \phi_i f(\omega t)$, where the subscript i indicates either the external (ex) or the gate electrode (el) potential. Assuming a thin electric double-layer regime (26, 27), and assuming that $1/\omega$ is longer than the charging time of the electric double layer, the EO slip velocity can be described by the Helmholtz–Smoluchowski relation (28),

$$u_{EOF}(t) = -\frac{\epsilon_l \zeta(t)}{\eta} E(t), \quad [1]$$

where ϵ_l is the dielectric permittivity of the liquid, η is its viscosity, $E(t) = V_{ex}(t)/L$ is the electric field in the chamber, and $\zeta(t)$ is

the zeta potential relative to the bulk. For $r_0 \ll L$, this bulk potential can be assumed to be uniform over the electrode and given by $V_{ch}(t) = (x_{el}/L) V_{ex}(t)$. Regardless of the specific model used to describe the electric double layer [e.g., Guoy–Chapman, Stern, Bockris, etc. (ref. 28)], the zeta potential can be described by some function G of the difference between the gate and this bulk potential, $\zeta(t) = G(V_{el}(t) - V_{ch}(t))$. Substituting the expression for $E(t)$ and $\zeta(t)$ into Eq. 1, the time-dependent EOF velocity can be expressed as

$$u_{EOF}(t) = -\frac{\epsilon_l}{\eta L} \phi_{ex} f(\omega t) G \left[\left(\phi_{el} - \frac{x_{el}}{L} \phi_{ex} \right) f(\omega t) \right]. \quad [2]$$

The time-averaged EOF velocity is obtained by integrating Eq. 2 over one time period which, for the case where f is a square-wave function (Fig. 1C), yields

$$u_{EOF}^{av}(\Delta\phi) = -\frac{1}{2} \frac{\epsilon_l}{\eta L} \phi_{ex} [G(\Delta\phi) - G(-\Delta\phi)], \quad [3]$$

where $\Delta\phi = \phi_{el} - (x_{el}/L)\phi_{ex}$ is the difference between the gate potential and bulk potential amplitudes. Eq. 3 shows that u_{EOF}^{av} is a symmetric function of $\Delta\phi$ regardless of the behavior of the function G . Fig. 1D shows an experimental measurement of the time-averaged EOF velocity as a function of the amplitude difference $\Delta\phi$, exhibiting the expected symmetry. We note that Eq. 3 is not valid outside the electrode region, where $\Delta\phi$ is not defined. In such regions the zeta potential can be assumed to be constant in time and related only to the native surface charge, and the time-averaged EOF therefore vanishes. In *SI Appendix* we provide a more generalized formulation of the system, accounting also for dc biases.

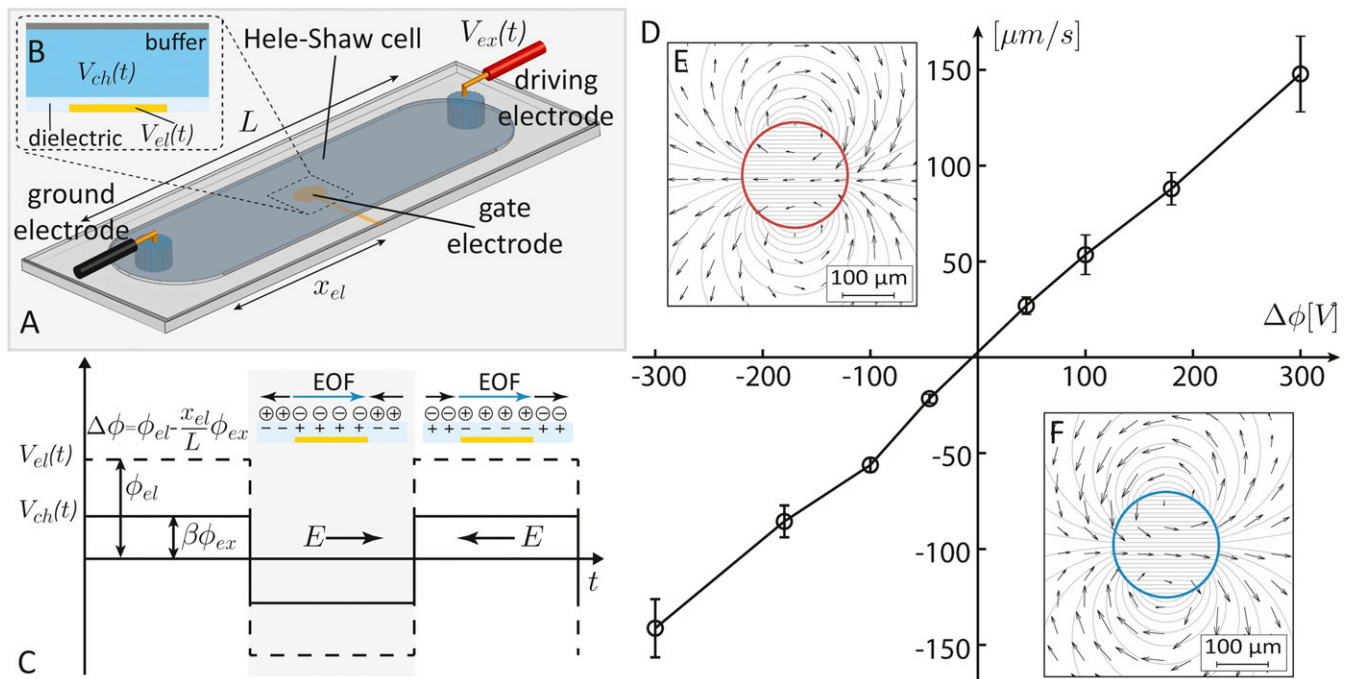


Fig. 1. Concept of shaping EOFs by using gate electrodes in a Hele–Shaw cell. (A) Illustration of the fluidic system consisting of a Hele–Shaw cell of length L , a ground- (Left) and a driving (Right) electrode placed in two separate reservoirs, and gate electrodes placed at a distance x_{el} from the ground electrode. (B) The gate electrode consists of a conductive layer insulated from the electrolyte in the chamber by a thin dielectric layer. (C) The potential of the driving electrode is set to a symmetric square-wave form of amplitude ϕ_{ex} . The gate-electrode potential is modulated in sync with the driving potential with an amplitude ϕ_{el} , resulting in a net EOF with intensity and directionality depending on the local amplitude difference $\Delta\phi = \phi_{el} - (x_{el}/L)\phi_{ex}$. The wave forms are here illustrated for the case of $\Delta\phi > 0$, for which the EOF is directed toward the driving electrode. (D) Experimental results showing the depth-averaged velocity as function of the applied gate potential for an electric field amplitude of $\phi_{ex}/L = 150\text{V/cm}$ as measured using a unidirectional flow configuration, as described in *Materials and Methods*. (E and F) Experimental (vector field) and analytical (streamlines) flow field of an EOF dipole generated by a 200- μm -diameter disc-shaped gate electrode for a negative and a positive $\Delta\phi$. Here the longest vector corresponds to a maximum velocity of 4.22 $\mu\text{m/s}$.

To achieve flow patterning using ac-FEEO, we use one or more spatially distributed gate electrodes. In the lubrication approximation ($L > r_0 \gg h$), any discrete electrode (regardless of its specific shape) results in dipole-like circulation flow (*SI Appendix*, Fig. S6). Therefore, the choice of a disk-shaped electrode is a natural one as the depth-average velocity \bar{u} can be described by a simple analytical expression (10),

$$\bar{u}(r, \theta, \Delta\phi) = \begin{cases} -\frac{\epsilon_l}{4\eta L} \phi_{ext} \frac{\zeta(\Delta\phi)}{2} \left(\frac{r_0}{r}\right)^2 [\cos\theta\hat{r} + \sin\theta\hat{\theta}] & r > r_0 \\ -\frac{\epsilon_l}{4\eta L} \phi_{ext} \frac{\zeta(\Delta\phi)}{2} [\cos\theta\hat{r} - \sin\theta\hat{\theta}] & r \leq r_0, \end{cases} \quad [4]$$

where r is the radial vector relative to the center of the disc and θ is the angle between r and the electric field. In our experimental setup $h = 15\mu\text{m}$, $r_0 \sim 100\mu\text{m}$, and $L \sim 1\text{ cm}$, satisfying the lubrication conditions.

Fig. 1 *E* and *F* shows the stream function (obtained from Eq. 4) for a negative and a positive $\Delta\phi$, respectively, together with the experimentally measured vector flow field, for a 200- μm -diameter disk-shaped gate electrode. This illustrates that the expected dipole flow can be obtained using the ac-FEEO mechanism and that the intensity and direction of the dipole can be indeed tuned by controlling $\Delta\phi$. *Movie S1* presents the visualization of this flow field during dynamic variation of $\Delta\phi$.

System Design and Characterization

Central to the operation of the ac-FEEO is the ability to maintain capacitive charging over the gate electrode for a large number of charge and discharge cycles under high-driving electric fields (order of 100 V/cm). Clearly, a thick dielectric layer would be ideal to insulate the electrode against Faradaic currents, thus preventing bubble formation and pH changes resulting from electrolysis. However, the thickness of the dielectric layer should also be chosen to maximize the effect of the gate electrode on the induced zeta potential. A good approximation for the surface zeta potential as a function of $\Delta\phi$ can be obtained from a capacitor model (12, 13, 15, 22, 28) accounting for the capacitance of the EDL ($C_{EDL} = \epsilon_l A / \lambda_{EDL}$) in series with the dielectric capacitance ($C_d = \epsilon_d A / d$),

$$\zeta = \zeta_0 + \frac{C_d}{C_{EDL}} \Delta\phi = \zeta_0 + \frac{\lambda_{EDL}}{\epsilon_l} \epsilon_d \frac{\Delta\phi}{d}, \quad [5]$$

where ζ_0 is the native zeta potential of the surface, and λ_{EDL} is the Debye length. Therefore, the most effective FEEO can be expected for a dielectric with the smallest possible thickness d and the largest possible permittivity ϵ_d . The best dielectrics can be obtained in standard microfabrication processes that (29) exhibit dielectric breakdown values on the order of 1 V/nm. Given that the EOF driving voltages in our system are in the range of 100–400 V, a 500-nm layer of a high-quality dielectric is expected to withstand such potential differences.

Fig. 2 shows the measured dielectric breakdown field (breakdown voltage normalized by the dielectric thickness) for different dielectric coatings deposited with plasma-enhanced chemical vapor deposition (PECVD). See *SI Appendix*, Fig. S5 for details of the experimental setup and additional measurements for layer deposited with atomic layer deposition. The dielectric is inherently in an asymmetric configuration as it is in contact with a metal on one side and an electrolyte on the other. Because under an ac field the dielectric will be subjected to both positive and negative voltages, it is important to measure its breakdown for both cases. Pure SiN_x shows poor dielectric resistance, holding only up to $\sim 0.1\text{ V/nm}$.

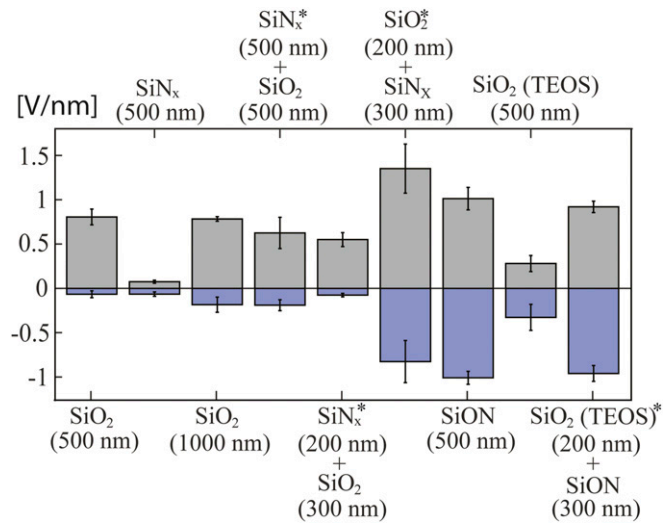


Fig. 2. Experimental characterization of the breakdown strength of different dielectric layers deposited with PECVD. For the case of two materials, the material indicated with an asterisk forms the layer in direct contact with the metal. The SiN_x layer shows the worst performance with a breakdown of $\sim 0.1\text{ V/nm}$; the SiO_2 layer shows an asymmetric behavior, holding up to $\sim 0.8\text{ V/nm}$ for positive potential ($\Delta\phi > 0$) but performing poorly for negative ones ($\Delta\phi < 0$). Using a layer of SiO_2 covered with a layer of SiN_x boosts significantly the breakdown strength, up to $\sim 1.3\text{ V/nm}$ for positive voltages; however, it shows poor repeatability (high error bars) and scarce symmetry. The best performance is obtained using SiON , withstanding up to $\sim 1\text{ V/nm}$ for both positive and negative voltages; therefore we choose SiON as insulating dielectric layer. The error bars represent the 95% confidence interval of the mean (with at least 10 repetitions).

SiO_2 performs significantly better for positive voltages, yet exhibits a clear asymmetry with a very low breakdown threshold for negative voltages ($\sim 0.1\text{ V/nm}$). Doubling the thickness of this layer to $1\mu\text{m}$ does not show an improvement. A two-layer composition of SiN_x on top of SiO_2 provides a significant improvement in both breakdown voltage and symmetry; however, we note that flipping the order of the layers is not equivalent and yields poor performance, even for large thicknesses. SiO_2 deposition using tetraethyl orthosilicate precursors show better symmetry but a lower absolute breakdown field. The dielectric that showed the best performance is SiON , yielding a 1-V/nm breakdown voltage for both positive and negative applied voltages; therefore, we use this layer composition as the baseline of this work and cover it with an additional 100-nm layer of SiO_2 because it has been well characterized for its EO properties (28).

The principle of ac-FEEO relies on the ability to synchronize the net charge in the double layer with the phase of the driving electric field. The upper bound on the frequency of the driving electric field is therefore dictated by the EDL charging time, which is a function of both the charge relaxation time within the electrolyte and any resistor–capacitor timescales associated with the electronics. Higher frequencies lead to reduced EOF as shown by van der Wouden et al. (24). *SI Appendix*, Fig. S5 presents the response of our system to a sudden change of applied gate voltage for different gate-electrode dimensions (see experimental details in *SI Appendix*). The observed timescale for the electrodes used in this work ($200 \times 200\mu\text{m}$), defined as the time needed for the gate current to drop to 10% of its initial value, is $\sim 5\text{ ms}$. The maximum ac frequency that could be used while still benefiting from a fully charged EDL is $\sim 200\text{ Hz}$, and we use this value as a frequency upper bound when operating our system. We note that the response of the system to positive and negative potentials is highly symmetric and we attribute this to the properties of the SiON layer used. This is in contrast to the asymmetric behavior of the SiO_2 layer reported by van der Wouden et al. (25).

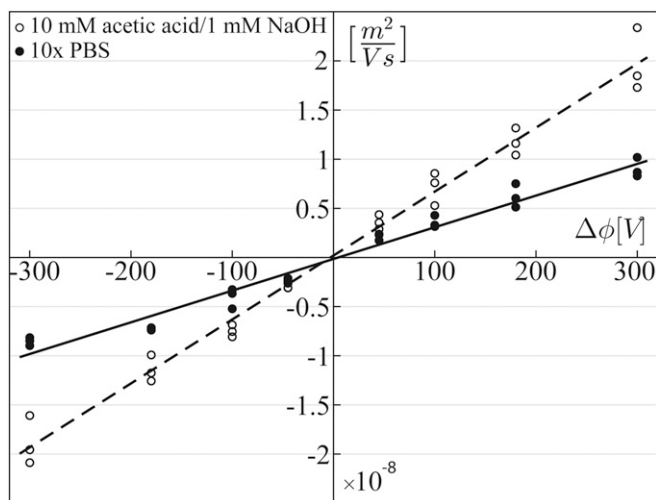


Fig. 3. Experimental results showing the time-averaged EO wall mobility as function of $\Delta\phi$ for different buffers: 10 mM acetic acid/1 mM NaOH (pH 3.8, 1.4×10^{-2} S/m, dashed line) and 10-times diluted PBS (pH 7.4, 2×10^{-1} S/m, continuous line). In this range of applied potentials, as expected from Eq. 5, both curves show a linear dependence, with R^2 values of 0.96 and 0.99, respectively. The experiments are performed using a straight channel with an array of gate electrodes and fluorescent beads to trace the flow; the EO wall mobility is derived by the depth-average velocity obtained by PIV.

A key advantage of using gate electrodes for controlling flows is the ability to switch from one flow pattern to another. The timescale associated with such switching is limited not only by the EDL charging process but also by the viscous response, $\tau_v = h^2/\nu$, where ν is the kinematic viscosity of the liquid. For a 15- μm -high chamber and an aqueous solution, as used in our experiments, $\tau_v \sim 0.2$ ms, significantly shorter than the electric response, thus not limiting the switching time. However, for $h \sim 100$ μm , τ_v is on the same order of magnitude of the EDL charging and could dominate the dynamic response of the system.

To complete the characterization of our system, Fig. 3 presents the measured time-averaged EO wall mobility ($\mu_{EO}^{av} = u_{EOF}^{av}/E$) as a function of the applied amplitude difference $\Delta\phi$. While, as expected, higher EO wall mobility is obtained using a low-pH buffer (10 mM acetic acid and 1 mM NaOH, pH 3.8), the use of physiological pH buffer (10 times diluted PBS) also provides significant EO mobility, indicating the potential use of ac-FEEO flow patterning for biochemical applications. Both curves show a linear dependence within this range of applied potentials, consistent with Eq. 5.

Dynamic Flow Patterning

Flow-field patterns can be obtained by superposition of flows generated by a distributed set of gate electrodes. The ability to individually address each electrode and dynamically modify its associated zeta potential allows switching from one flow pattern to another in real time. Fig. 4 demonstrates this concept for a basic case of two 200- μm -diameter disc-shaped gate electrodes. At t_1 (Fig. 4D), the electrodes are assigned $\Delta\phi$ values of +80 V (left electrode) and -80 V (right electrode), resulting in two dipoles with equal and opposite strengths, generating an EOF quadrupole. At t_2 (Fig. 4E), we change the $\Delta\phi$ value on the left electrode to 0 V, thus effectively eliminating its influence. At t_3 (Fig. 4F), we match the $\Delta\phi$ of the left electrode to the one on the right, resulting in a nested dipole configuration, consisting of recirculating flow around each electrode and a larger-scale recirculation between the two electrodes. The images presented here correspond to three time points of a continuous movie provided as [Movie S2](#). These flow patterns can be well predicted by using Eq. 4 as shown in Fig. 4 A–C.

A particularly interesting configuration consists of two concentric electrodes, i.e., a disc-shaped electrode (inner) of radius R_{in} surrounded by an annulus-shaped one (outer) having an outer radius R_{out} . For such a case, theory predicts that setting $\Delta\phi_{in} = [(R_{out}/R_{in})^2 - 1]\Delta\phi_{out}$ would result in an internal recirculation while maintaining zero velocity outside the outer electrode (Fig. 5B). Fig. 5A demonstrates the implementation of this configuration, showing that such a bounded flow field is indeed feasible. Some “leakage” of the flow field is however observed in the experiments; this is due to the imperfection of the annulus shape that contains a slit serving as a path for the electrical connection to the inner disc. Furthermore, the existence of the electrical lines themselves adds an additional perturbation to the flow. These perturbations also exist in Fig. 4 but they are less visible there because the velocity field magnitude is substantial compared with such perturbations. Setting $\Delta\phi_{in} = 0$ V (Fig. 5 C and D) switches the flow field to a unique configuration in which a pressure jump at the outer edges of the annulus is compensated by an opposite pressure jump at the inner edges, leaving the inner region free of both slip velocity and pressure gradients. As a result, in the inner region the velocity field is uniformly zero, thus creating a finite stagnation volume within the flow.

Dynamic Streamlines Shaping

A set of gate electrodes can also serve as an effective way of shaping existing flow fields created by, for example, pressure-driven flow or dc EOF. Fig. 6 shows the effect of a 2×4 array of disc-shaped electrodes on uniform flow generated by a pressure gradient. At t_1 , we activate the electrode array, assigning two values of $\Delta\phi$, a positive and a negative one, in a checkerboard

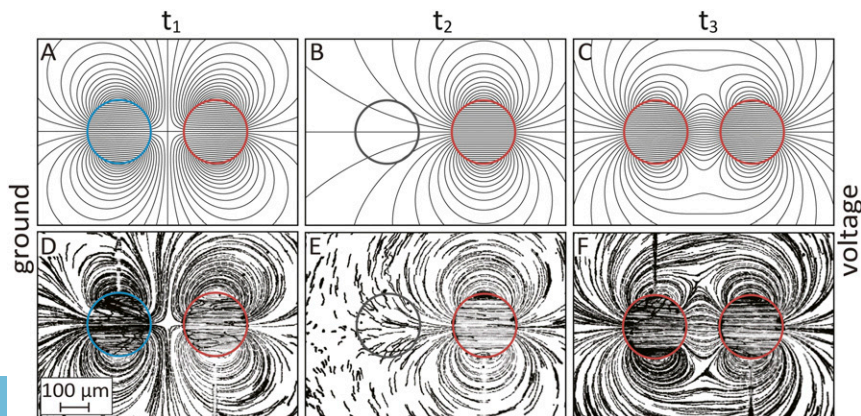


Fig. 4. Analytical predictions and experimental visualization of flow streamlines generated by two 200- μm -diameter disc-shaped gate electrodes for different $\Delta\phi$ combinations. (A and D) At t_1 , we set the electrodes to opposite $\Delta\phi$ values, generating opposing dipoles and resulting in a quadrupole flow field. (B and E) At t_2 , we switch the $\Delta\phi$ of the left electrode to zero, effectively eliminating its effect on the flow. (C and F) At t_3 , we match the $\Delta\phi$ of both electrodes, resulting in a flow configuration having two regions of local recirculation nested within a larger recirculating flow. The driving amplitude is $\phi_{ex} = 200$ V, and because the electrodes are located at the center of the chamber $\phi_{ch} \sim 100$ V. A time-lapse movie showing the flow fields and the transition between them is provided in [Movie S2](#).

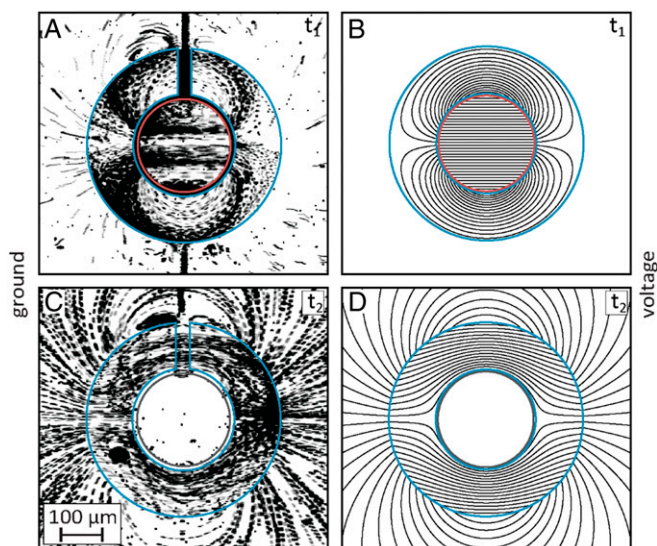


Fig. 5. Analytical predictions and experimental visualization of flow streamlines generated by a 200- μm -diameter disc-shaped electrode surrounded by a 400- μm -outer-diameter annulus, for different $\Delta\phi$ combinations. (A and C) At t_1 , the potential amplitude ratio of the two gate electrodes is set such that outside the annulus the two EOF dipoles cancel each other (inner $\Delta\phi = -120$ V and outer $\Delta\phi = 40$ V), resulting in an isolated region of recirculating flow surrounded by a quiescent liquid. (B and D) At t_2 , we set the $\Delta\phi$ of the disc electrode to zero, and demonstrate the opposite case of a finite stagnation volume surrounded by flow. The amplitude in the channel for both case is $\phi_{ex} = 300$ V, and approximately $\phi_{ch} = 160$ V in the electrode region. A time-lapse movie showing the flow fields and the transition between them is provided in [Movie S4](#).

pattern. As expected from our theoretical predictions, the velocity components perpendicular to the electric fields bend the incoming flow, resulting in a sinusoidal streamline. At t_2 , we set $\Delta\phi = 0$ to all electrodes and the flow field relaxes back to its original state. At t_3 , we invert the checkerboard pattern, resulting again in a sinusoidal shape but with a phase shifted by 180° . In the simulation, the incoming velocity field was set to $40 \mu\text{m/s}$ to match the experiments, and the slip velocities of the electrodes were tuned to obtain the desired flow pattern. Through the use of the independent measurements of the EO wall mobility reported in Fig. 3, these slip

velocities were translated to $\Delta\phi$ values, which were then used in the experiments with no additional fitting parameters. As shown in Fig. 6, the agreement between theory and measurements is not only qualitative but also quantitative, showing the streamlines being deflected to the same extent.

Such flow shaping can also be integrated as part of more elaborated devices. As an example, Fig. 7 shows the use of two electrodes to deflect a central inlet streamline into one of the three possible outlets. At t_1 , the electrodes are set to create a counterclockwise flow, thus deflecting the incoming streamline toward the lower outlet. At t_2 , both the electrodes are set to have a $\Delta\phi = 0$; the streamline enters the central outlet undisturbed. At t_3 , we set the electrodes to create a clockwise velocity pattern, thus routing the streamline to the upper outlet.

Conclusion and Outlook

We presented the use of ac-FEEO as a mechanism to create dynamic flow patterns in a Hele–Shaw configuration. We showed that the basic flow pattern of an EOF dipole predicted by the theory can be experimentally reproduced by this mechanism, with dipole strength set by the voltage amplitude difference between the electrode and the bulk. In contrast to zeta-potential modification using chemical patterning (11, 30), electric control allows setting the values of EOF within a continuous range of positive and negative values, and to rapidly switch between them. The timescale for such switching depends on the EDL charging time and the viscous time, which in our system is on the order of 5 ms. We investigated several electrode configurations and demonstrated a variety of flow patterns that can be realized. To the best of our knowledge, some of these patterns, such as the localized recirculation and the stagnation volume, have not been demonstrated by other means. Furthermore, we showed that ac-FEEO can interact with existing flow fields and dynamically tune their streamlines.

Precise microscale flow control may be useful in several applications. For example, whereas large particles can be manipulated in microsystems by other mechanisms such as dielectrophoresis or optical tweezers, controlled transport of small molecules remains challenging. The technique presented here could be particularly useful to bridge this gap, and allow control of the mass transport of small chemicals and biomolecules such as proteins, DNA, peptides, etc. Because this technique drives the fluid itself and not the single particles, it may be useful for heat-transfer management in microdevices, and the pressure field formed may be leveraged

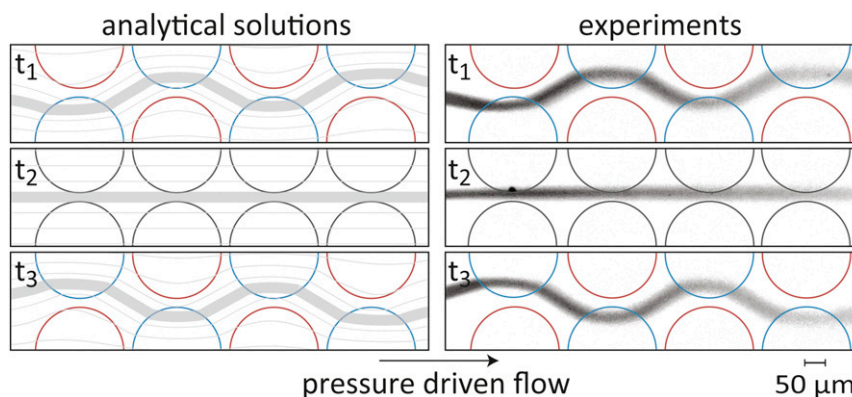


Fig. 6. Analytical predictions and experimental visualization of flow-field shaping using a 2×4 array of gate electrodes. We establish a uniform flow in the chamber by pressure gradient and at t_1 , we set the electrode potentials to a checkerboard pattern with values of $\Delta\phi = 150$ V and $\Delta\phi = -150$ V and an external amplitude to $\phi_{ex} = 300$ V. The multiple dipoles superpose with the uniform flow, resulting in sinusoidal shaping of the central streamline. When the gate potentials are set to zero (t_2) the flow relaxes to its original shape. At t_3 , we flip the original checkerboard pattern, obtaining a sinusoidal shape with a shifted phase. The gate potential values used in the experiments are derived from theoretical predictions together with the calibration curve of Fig. 3, with no additional fitting parameters. A time-lapse movie showing the evolution of the streamline formation is provided in [Movie S5](#).

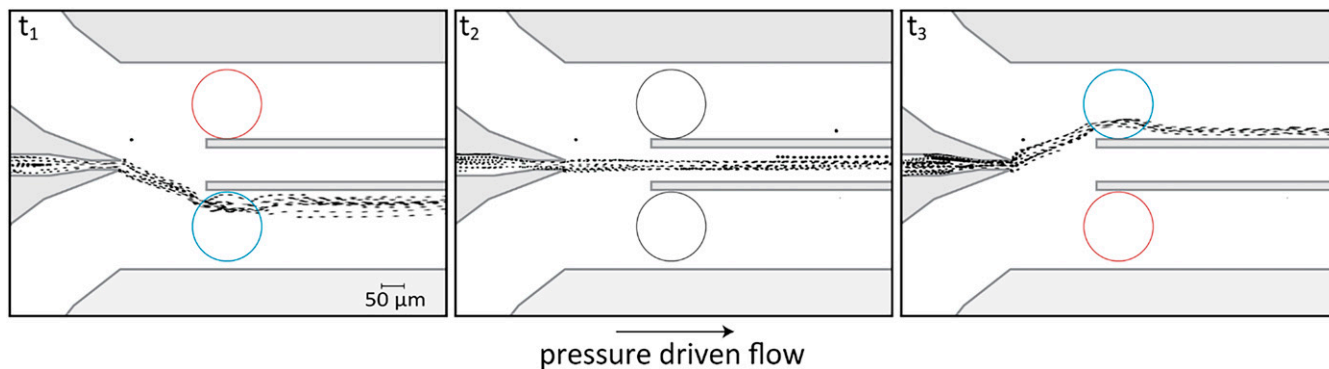


Fig. 7. Demonstration of flow-field shaping integrated in a microfluidic device. The gate electrodes can be used to shape an existing flow field and direct an incoming streamline into one of the three outlets. At t_1 , we impose $\Delta\phi = -310\text{V}$ and $\Delta\phi = 350\text{V}$ to the top and bottom electrode, respectively, to induce a counterclockwise velocity field, thus pushing the streamline to the bottom outlet. At t_2 , we set a $\Delta\phi = 0$ to both electrodes and the flow returns to its native state, with the central streamline continuing to the central outlet undisturbed. At t_3 , we flip the initial $\Delta\phi$ assignment to the electrodes directing the streamline to the upper outlet. A time-lapse movie showing this switching process is provided in [Movie S6](#).

to actuate deformable surfaces, such as free surfaces or elastic actuators. In this work, we used few individual electrodes providing access to only a limited set of flow patterns. An ideal flow control system would allow any desired flow pattern on a large scale. One could envision such a system constructed from a large number of individually addressed electrodes, likely in array format.

Materials and Methods

We characterized the EOF velocity as a function of the applied amplitude difference $\Delta\phi$. We used a 100- μm -wide, 15- μm -high, and 1-cm-long straight channel containing an array of gate electrodes distributed over the entire length of the channel and composed of $100 \times 100\text{-}\mu\text{m}^2$ units, spaced 10 μm edge to edge. These gate electrodes are set to give an equal $\Delta\phi$ along the channel to ensure a homogeneous EOF slip velocity throughout the channel. We measured the depth-averaged velocity by particle image velocimetry (PIV) analysis, using 0.8- μm carboxyl fluorescent particles (Spherotech Inc.) as flow tracer and PIVlab for the image analysis. Assuming a pure Couette-type

flow, we estimate the slip velocity to be twice the measured depth-averaged velocity, and use this to calculate the velocity (shown in Fig. 1D) and the EO wall mobility (shown in Fig. 3) via the Helmholtz-Smoluchowski relation.

Additional information on visualization conditions, image analysis, and device fabrication is provided in [SI Appendix](#).

ACKNOWLEDGMENTS. We thank S. Dehe for introducing us to the work of van der Wouden et al. (24, 25) on ac-based actuation; S. Dehe and B. Rofman for further useful discussions on this topic; E. Boyko, D. Taylor, X. van Kooten, and Y. Temiz for useful discussions; D. Dávila Pineda and U. Drechsler for continuous help and support on the microfabrication; and S. Rubin and K. Gommel for collaboration on early attempts using dc actuation. F.P., V.B., and G.V.K. acknowledge P. Renaud, E. Delamarche, and W. Reiss for their continuous support. F.P. was supported by the Initial Training Network, Virtual Vials, funded by the FP7 Marie Curie Actions of the European Commission (FP7-PEOPLE-2013-ITN-607322). This project has received funding from the European Research Council under the European Union's Horizon 2020 Research and Innovation Programme, Grant agreement 678734 (MetamorphChip).

- Stone HA, Stroock AD, Ajdari A (2004) Engineering flows in small devices: Microfluidics toward a lab-on-a-chip. *Annu Rev Fluid Mech* 36:381–411.
- Nguyen N-T (2010) Micro-optofluidic lenses: A review. *Biomicrofluidics* 4:031501.
- Psaltis D, Quake SR, Yang C (2006) Developing optofluidic technology through the fusion of microfluidics and optics. *Nature* 442:381–386.
- Pennathur S, Eijkel JCT, van den Berg A (2007) Energy conversion in microsystems: Is there a role for micro/nanofluidics? *Lab Chip* 7:1234–1237.
- Chen X, Xu B, Liu L (2014) Nanoscale fluid mechanics and energy conversion. *Appl Mech Rev* 66:050803.
- Choi K, Ng AHC, Fobel R, Wheeler AR (2012) Digital microfluidics. *Annu Rev Anal Chem (Palo Alto Calif)* 5:413–440.
- Jones TB, Gunji M, Washizu M, Feldman MJ (2001) Dielectrophoretic liquid actuation and nanodroplet formation. *J Appl Phys* 89:1441–1448.
- Darhuber AA, Valentino JP, Davis JM, Troian SM, Wagner S (2003) Microfluidic actuation by modulation of surface stresses. *Appl Phys Lett* 82:657–659.
- Oh KW, Ahn CH (2006) A review of microvalves. *J Micromech Microeng* 16:R13–R39.
- Boyko E, Rubin S, Gat AD, Bercovici M (2015) Flow patterning in Hele-Shaw configurations using non-uniform electro-osmotic slip. *Phys Fluids* 27:102001.
- Paratore F, Boyko E, Gat AD, Kaigala GV, Bercovici M (2018) Toward microscale flow control using non-uniform electro-osmotic flow. *Proceedings SPIE BiOS: Microfluidics, BioMEMS, and Medical Microsystems XVI* (International Society for Optics and Photonics, Bellingham, WA), Vol 10491. Available at <https://www.spiedigitallibrary.org/conference-proceedings-of-spie/10491/104910P/Toward-microscale-flow-control-using-non-uniform-electro-osmotic-flow/10.1117/12.2300963.short?SSO=1>. Accessed February 19, 2018.
- Ghowsi K, Gale RJ (1990) Application of field effect electro-osmosis to separation-based sensors. *Biosensor Technology Fundamentals and Applications*, ed Buck RP (Routledge, Abingdon, UK).
- Lee CS, Blanchard WC, Wu CT (1990) Direct control of the electroosmosis in capillary zone electrophoresis by using an external electric field. *Anal Chem* 62:1550–1552.
- Hayes MA, Ewing AG (1992) Electroosmotic flow control and monitoring with an applied radial voltage for capillary zone electrophoresis. *Anal Chem* 64:512–516.
- Wu CT, Lopes T, Patel B, Lee CS (1992) Effect of direct control of electroosmosis on peptide and protein separations in capillary electrophoresis. *Anal Chem* 64:886–891.
- Wu CT, Huang TL, Lee CS, Miller CJ (1993) Dispersion studies of capillary electrophoresis with direct control of electroosmosis. *Anal Chem* 65:568–571.
- Schasfoort RBM, Schlautmann S, Hendrikse J, van den Berg A (1999) Field-effect flow control for microfabricated fluidic networks. *Science* 286:942–945.
- Sniadecki NJ, Lee CS, Sivanesan P, DeVoe DL (2004) Induced pressure pumping in polymer microchannels via field-effect flow control. *Anal Chem* 76:1942–1947.
- Buch JS, Wang P-C, DeVoe DL, Lee CS (2001) Field-effect flow control in a polydimethylsiloxane-based microfluidic system. *Electrophoresis* 22:3902–3907.
- Polson NA, Hayes MA (2000) Electroosmotic flow control of fluids on a capillary electrophoresis microdevice using an applied external voltage. *Anal Chem* 72:1088–1092.
- Horiuchi K, Dutta P (2006) Electrokinetic flow control in microfluidic chips using a field-effect transistor. *Lab Chip* 6:714–723.
- Hayes MA, Kheterpal I, Ewing AG (1993) Effects of buffer pH on electroosmotic flow control by an applied radial voltage for capillary zone electrophoresis. *Anal Chem* 65:27–31.
- Muthu S, Svec F, Mastrangelo CH, Frechet JMJ, Gianchandani YB (2004) Enhanced electro-osmotic pumping with liquid bridge and field effect flow rectification. *17th IEEE International Conference on Micro Electro Mechanical Systems. Maastricht MEMS 2004 Technical Digest* (IEEE, New York), pp 850–853.
- van der Wouden EJ, Pennathur S, van den Berg A (2008) AC field effect flow control of EOF in complex microfluidics systems with integrated electrodes. *12th International Conference on Miniaturized Systems for Chemistry and Life Sciences*, San Diego (Chemical and Biological Microsystems Society, San Diego), pp 721–723.
- van der Wouden EJ, Hermes DC, Gardeniers JGE, van den Berg A (2006) Directional flow induced by synchronized longitudinal and zeta-potential controlling AC-electrical fields. *Lab Chip* 6:1300–1305.
- Ajdari A (1995) Electro-osmosis on inhomogeneously charged surfaces. *Phys Rev Lett* 75:755–758.
- Ajdari A (1996) Generation of transverse fluid currents and forces by an electric field: Electro-osmosis on charge-modulated and undulated surfaces. *Phys Rev E Stat Phys Plasmas Fluids Relat Interdiscip Topics* 53:4996–5005.
- Hunter RJ (1988) *Zeta Potential in Colloid Science: Principles and Applications* (Academic, London).
- Rymaszewski EI (1997) Properties needed for electronic and magnetic applications. *ASM Handbook: Materials Selection and Design*, ed Dieter GE (ASM International, Novato, OH), pp 615–621.
- Stroock AD, et al. (2000) Patterning electro-osmotic flow with patterned surface charge. *Phys Rev Lett* 84:3314–3317.